Mispointing characterization and Doppler velocity correction for the conically scanning WIVERN Doppler radar

Filippo Emilio Scarsi[1,2], Alessandro Battaglia[1,3,4], Frederic Tridon[1], Paolo Martire[1], Ranvir Dhillon[3], and Anthony Illingworth[5]

[1]Politecnico of Torino, Torino, Italy
[2]University School for Advanced Studies IUSS Pavia, Pavia, Italy
[3]University of Leicester, Leicester, UK
[4]National Centre for Earth Observation, Leicester, UK
[5]University of Reading, Reading, UK

Correspondence: Filippo Emilio Scarsi
filippo.scarsi@polito.it

Abstract. Global measurements of horizontal winds in cloud and precipitating systems represent a gap in the global observing system. The WIVERN mission, one of the two candidates to be the ESA's Earth Explorer 11 mission, aims at filling this gap based on a conically scanning W-band Doppler radar instrument. The determination of the antenna boresight mispointing angles and the impact of their uncertainty on the line of sight Doppler velocities is critical to achieve the mission requirements.

5 While substantial industrial efforts are on their ways for achieving accurate determination of the pointing, alternative (external) calibration approaches are currently under scrutiny. The correction of the line of sight Doppler velocity error introduced by the mispointing only needs knowledge of such mispointing angles and does not need the correction of the mispointing itself. Thus, this work discusses four methods applicable to the WIVERN radar that can be used at different time scales to characterize the antenna mispointing both in the azimuthal and in the elevation directions and to correct the error in the Doppler velocity

10 induced by such mispointing.

Results show that elevation mispointing is well corrected at very short time scales by monitoring the range at which the surface peak occurs. Azimuthal mispointing is harder but can be tackled by using the expected profiles of the non-moving surface Doppler velocity. Biases in pointing at longer time scales can be monitored by using a well established reference database (e.g. ECMWF reanalysis) or ad-hoc ground based calibrators.

15 Although tailored to the WIVERN mission, the proposed methodologies can be extended to other Doppler concepts featuring conically scanning or slant viewing Doppler systems.

1 Introduction

Global observations of horizontal winds are of great scientific importance and have huge economic impact (Stoffelen et al., 2020). This has been widely demonstrated by the ESA Aeolus mission (Stoffelen et al., 2005), the first ever satellite mission to deliver profiles of Earth's wind in the lowermost 30 km of the atmosphere on a global scale, via the measurement of the Doppler shifts in the ALADIN (Atmospheric LAser Doppler INstrument) ultraviolet lidar backscattered signals (ESA, 2008; Lux et al., 2021). Though Aelous contributes less than 1 % inputs in numerical weather prediction (NWP), it significantly improves short-range forecasts as confirmed by observations sensitive to temperature, wind and humidity (Rennie et al., 2021). Note that Aeolus only measures winds in clear sky (so called "Rayleigh winds") and inside thin clouds ("Mie winds"). Scatterometer measurements can also provide complementary observations at the surface, with significant progress being recently achieved even in presence of strong winds near heavy rain (Polverari et al., 2022). Similarly, winds at cloud top can be derived from successive satellite images of clouds and humidity, the so-called Atmospheric Motion Vectors. However, apart from sporadic and sparse radio soundings and aircraft penetrations, no wind observations are currently available inside thick clouds and precipitating systems. Recent advances in data assimilation systems have demonstrated that the dynamical state of the atmosphere can be inferred not only from clear sky temperature and relative humidity observations but also from observations in presence of clouds and precipitation (Geer et al., 2017). With clouds covering roughly 30 % of the tropospheric volume, Doppler cloud radars have the potential to complement wind observations by Doppler lidar in clear-sky and thin cloud conditions. To fulfil this goal, Illingworth et al. (2018) proposed the WInd VElocity Radar Nephoscope (WIVERN, www.wivern.polito.it) hinged upon a single instrument: a conically scanning W-band polarization diversity Doppler radar. The concept is currently undergoing Phase 0 studies as part of the ESA Earth Explorer 11 selection program.

Doppler radar measurements from low Earth orbit satellites are challenging (Tanelli et al., 2002; Battaglia et al., 2020; Kollias et al., 2022). In fact, the large spacecraft velocity (typically, in low Earth Orbit, it is of the order of 7.6 km s^{-1}), has a threefold repercussion.

1. In combination with a finite antenna beamwidth, it causes "satellite Doppler fading", i.e. a broadening of the Doppler spectrum, which is a synonym of a decreased medium correlation time (Kobayashi et al., 2002). This generally increases the uncertainties in the Doppler estimates performed with radar pulse pair estimators (Doviak and Zrnić, 1993). In order to mitigate this issue, techniques based on polarization diversity (Battaglia et al., 2013; Wolde et al., 2019) and Displaced Phase Center Antenna (Durden et al. (2007); Tanelli et al. (2016); Kollias et al. (2022)) concepts have been proposed.

2. In presence of inhomogeneity within the radar backscattering volume, it introduces non uniform beam filling biases (Tanelli et al., 2002; Kollias et al., 2014; Sy et al., 2014).

3. It requires a very precise and accurate knowledge of the antenna pointing to enable the subtraction of the non-geophysical component of the satellite velocity along the line of sight (Tanelli et al., 2004; Battaglia and Kollias, 2014).

The different sources of errors involved with a conically scanning Doppler radar with polarization diversity, as adopted for WIVERN, have been thoroughly discussed in Battaglia et al. (2018, 2022) and Rizik et al. (2023). End to end simulations

suggest that the WIVERN mission requirements on horizontal-projected line of sight winds, of a total random (systematic) error lower than 3 (0.5) m/s at an integration distance of 20 km for reflectivities above -15 dBZ, are at reach. Such accuracy is expected to be sufficient to ensure significant impact in operational NWP.

In previous error budget studies, antenna mispointing errors have been considered negligible in the overall error budget (i.e. $\lesssim 0.3$ m/s both for bias and random error, e.g. see Fig. 11 in Battaglia et al. (2022)). Phase 0 industry studies suggest that the mispointing power spectral density (PSD) has indeed larger components than previously expected, particularly for very slow varying components. This is due to a predicted larger uncertainty on the knowledge of the antenna boresight alignment after the launch compared to pre-launch ground measurements. Therefore the different error contributions have been classified and assigned to systematic errors or random errors according to the split frequency of 1.16e-5 Hz (which corresponds to 1 day period). In order to fulfill the mission requirements, when accounting for the other contributions (pulse pair estimator error, non uniform beam filling, wind shear, see Tridon et al. (2023)) the pointing contribution of the random line of sight (LoS) Doppler velocity error budget must be of the order of 0.4-0.6 m/s whereas the requirement for the systematic contribution has to be smaller than 0.3-0.6 m/s. At the moment, these latter figures are far from being achieved (of the order of 1.7 and 5.6 m/s for the two industrial consortia, ESA (2023)).

For the purpose of the mission (i.e. measuring accurate Doppler velocities), it is not paramount to have an accurate and precise pointing, but it is essential to achieve pointing knowledge within tens of microradians. Thus, methodologies to quantify the antenna mispointing are highly desired in the context of the WIVERN mission and in general for scanning atmospheric Doppler radars. In this paper, after introducing the geometry of observation and the impact of mispointing errors on LoS Doppler velocities (Sect. 2), different Doppler velocity correction methods are proposed and reviewed, discussing their potential for reducing the mispointing errors (Sect. 3). Conclusions and future work are outlined in Sect. 4. The methods described in the paper characterize the antenna mispointing angles and correct the error in the Doppler velocity induced by such mispointings. These methodologies do not correct the antenna pointing itself.

2 Mispointing errors

Fig. 1 depicts the geometry of observation of the WIVERN radar, whose specifics are listed in Tab. 1. Mispointing in the knowledge of the antenna boresight produces error in the estimates of the hydrometeor Doppler velocity, v_D, because the component of the spacecraft (SC) velocity, v_{SC}, along the antenna boresight needs to be subtracted from the measured Doppler velocity, v_{mD}: $v_D = v_{mD} - v_{SC}\sin(\theta)\cos(\phi)$, with the last term representing the projection of v_{SC} along the antenna boresight. If the actual pointing of the antenna has a mispointing of $\delta\theta$ in the elevation angle and of $\delta\phi$ in the azimuthal, then the mispointing error in Doppler velocity δv_{mis} will be:

$$
\begin{aligned}
\delta v_{mis} &= [v_{mD} - v_{SC}\sin(\theta)\cos(\phi)] - [v_{mD} - v_{SC}\sin(\theta+\delta\theta)\cos(\phi+\delta\phi)] \\
\frac{\delta v_{mis}}{v_{SC}} &= [\sin(\theta+\delta\theta)\cos(\phi+\delta\phi) - \sin(\theta)\cos(\phi)] = [(\sin(\theta)+\cos(\theta)\delta\theta)(\cos(\phi)-\sin(\phi)\delta\phi) - \sin(\theta)\cos(\phi)] \\
\delta v_{mis} &= v_{SC}[-\sin(\theta)\sin(\phi)\delta\phi + \cos(\theta)\cos(\phi)\delta\theta]
\end{aligned}
\tag{1}
$$
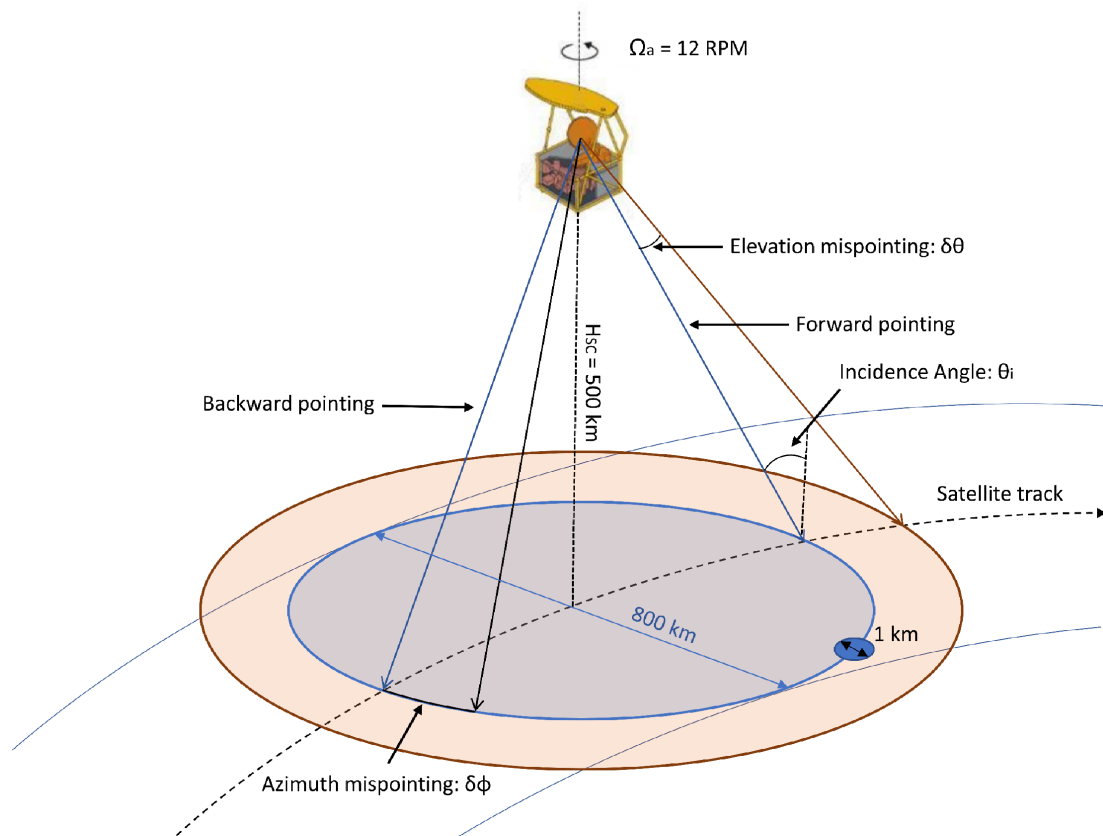
Figure 1. Geometry of observation of the WIVERN conically scanning radar: the antenna boresight, indicated by a thin blue line, is rotating at 12 RPM and pointing at a nominal incidence angle of about $42°$. The orange and the black arrows represent an elevation and an azimuthal mispointing in correspondence to the forward and backward pointing configuration, respectively.

where the azimuthal scanning angle is assumed $0°$ in the forward direction. Eq. 1 implies that the error in the LOS velocity is modulated by the azimuthal scan frequency since $\phi = \Omega_a t + \phi_0$, where $\Omega_a = 1.26$ rad/s is the antenna angular velocity. Note that a $100\,\mu$rad error in azimuth (elevation) produces a maximum error of 0.5 (0.57) m/s when looking sideways (forward/backward direction). Note that the sideways directions correspond to $\phi = \pm\pi/2$, and the forward and backward directions to $\phi = 0$ and $\phi = \pi$, respectively. Finally, it is important to highlight that in Eq. (1) and in the following discussion the antenna rotation axis is assumed vertical; the impact of a scan axis mounting offset is discussed in Sect. A.

3 Doppler velocity correction methods

Four different methods have been identified that can be used to correct Doppler velocity errors. Methods II and III are applicable both to azimuth and elevation mispointing, method I is applicable only to elevation mispointing and method IV only to

azimuthal mispointing; the first two (I and II) are effective on short time scales (of the order of few ms), the latter two (III and IV) on much longer time scales (weeks/months).

3.1 Correction method I: altimeter mode technique

95 Because of its peculiar illumination geometry, pulse shape and the receiver IF filter response (Meneghini and Kozu (1990)), the WIVERN radar will produce a very specific reflectivity shape for flat surfaces in absence of low level clouds and/or precipitation, with a peak corresponding to the surface range along the boresight direction (Battaglia et al. (2017); Illingworth et al. (2020)). Since the position of the spacecraft is extremely well known, any discrepancy δz between the range of the surface from the spacecraft computed along the (attitude and orbital control system (AOCS) - estimated) boresight direction and the

100 measured range of the surface peak can be attributed to an elevation mispointing, $\delta\theta$, from:

$$\delta\theta = \frac{\delta z}{r_{SC} \sin\theta_i} \approx \frac{\delta z \, \cos\theta_i}{\sin\theta_i \, H_{SC}} \tag{2}$$

where r_{SC} is the distance between the surface and the spacecraft along the boresight and H_{SC} is the spacecraft altitude. With the WIVERN specifics (see Tab. 1), a $\delta z = 10$ m corresponds to about 22.5 μrad. Unfortunately, this method is not viable for tackling the azimuth mispointing, but has the advantage that it depends only on the reflectivity profile, thus it has the same

105 sensitivity in each part of the scan.

In order to understand the uncertainties associated with this method, realistic surface returns as detected by WIVERN have been simulated starting from the expected flat surface return shape derived following Meneghini and Kozu (1990) (Fig. 5 in Illingworth et al. (2020); an example of a surface return is provided in Fig. 2, black line). The profiles have been scaled in order to produce different Peak to Noise Ratios (PNR), defined as the ratio between the peak reflectivity of the surface profile and

110 the single pulse sensitivity or reflectivity equivalent noise level of the radar, assumed to be equal to -15 dBZ. For each PNR and each integration length (with 8 independent pulses per km), different stochastic realizations of the signal plus the noise are simulated following the technique proposed by Zrnic (1975). One of such possible realizations is shown as the orange dashed line in Fig.2. Then the signal is noise subtracted (similarly to the method described in (Kollias et al., 2023)) and sampled at the WIVERN sampling rate (100 m along the range, see Tab. 1) with random range offsets in order to account for the variability of

115 the digitization process along the orbit (red diamonds in Fig. 2). A surface detection criterion is introduced. For each profile, only points that are 3 dB above the detection level (red diamonds with black points inside) are considered. If the profile contains at least 10 consecutive points above the detection threshold, it is then used for fitting the surface return shape with two free parameters: the peak height and the peak amplitude. The fit is performed via a least mean square procedure where each point is weighted by the expected error (errorbars in Fig. 2) computed according to the signal to noise ratio (SNR, following Eq. 16

120 in Battaglia et al. (2022)). The best fitting curve (blue line) differs from the actual profile for a shift in height, δz, and a shift in amplitude, δZ. The variability of δz can be statistically retrieved as a function of the PNR by generating a sufficient number of profile realizations with different random noise and different digitalizations of the signal. While, as expected (not shown), the mean value of δz over different digitization and stochastic noise is practically close to 0 m for every PNR and for every integration length, its standard deviation, $\sigma_{\delta z}$, decreases when either the PNR and/or the integration length increase, as shown

Table 1. Specifics of the WIVERN radar. The configuration here adopted is the one currently under Phase-0 study for the ESA Earth Explorer 11 program.

Spacecraft height, H_{SC}	500 km
Spacecraft velocity, v_{SC}	7600 ms^{-1}
Off-nadir pointing angle	38°
Incidence angle, θ_i	41.6°
RF output frequency	94.05 GHz
Transmitted power P_t	2 kW
Pulse width τ	3.3 μs
Antenna beamwidth, θ_{3dB}	1200 μrad
Circular antenna diameter	3 m
Antenna angular velocity, Ω_a	12 rpm
Footprint speed	500 kms^{-1}
Transmit polarization	H or V
Cross-polar isolation	<-25 dB
Single pulse sensitivity	-15 dBZ
H-V Pair Repetition Frequency	4 kHz
Range sampling distance (rate)	100 m (1.5 MHz)
Number of H-V Pairs per 1 km integration length	8

125 in Fig. 3. The shifts in elevation angle $\delta\theta$ corresponding to the shifting in altitude δz of the peak are reported on the y-axis on the right hand side of Fig. 3. For instance, with a PNR of 10 dB, the surface position is expected to be determined with an error of about 32, 20, 13 and 9 m for integration lengths of 1, 2, 5, 10 km, respectively. These values correspond to an uncertainty in elevation of 75, 47, 39 and 20 μrad. According to Eq. 1, the last three solutions guarantee that the velocity error induced by such mispointing will always remain below 0.3 m/s.

130 ### 3.1.1 Statistics of useful surface return

Estimates of the frequency of surfaces exceeding threshold values of PNR have been obtained by exploiting the climatology gathered by the polar-orbiting nadir-pointing CloudSat W-band radar and simulating the WIVERN returns at slant incidence angle. The method, proposed by Battaglia et al. (2018) and refined in Tridon et al. (2023), accounts for the additional path integrated attenuation and the reduction in surface normalised backscattering cross sections (Battaglia et al., 2017) when
135 considering the slanted viewing geometry of the WIVERN radar. Fig. 4 shows the cumulative distribution functions (cdf) of the surface peaks (and equivalently of PNR) for land and ocean surfaces. Since ocean surfaces are far less bright than land surfaces at WIVERN incidence angles, a lower percentage of sea than land surface profiles exceeds any given threshold.
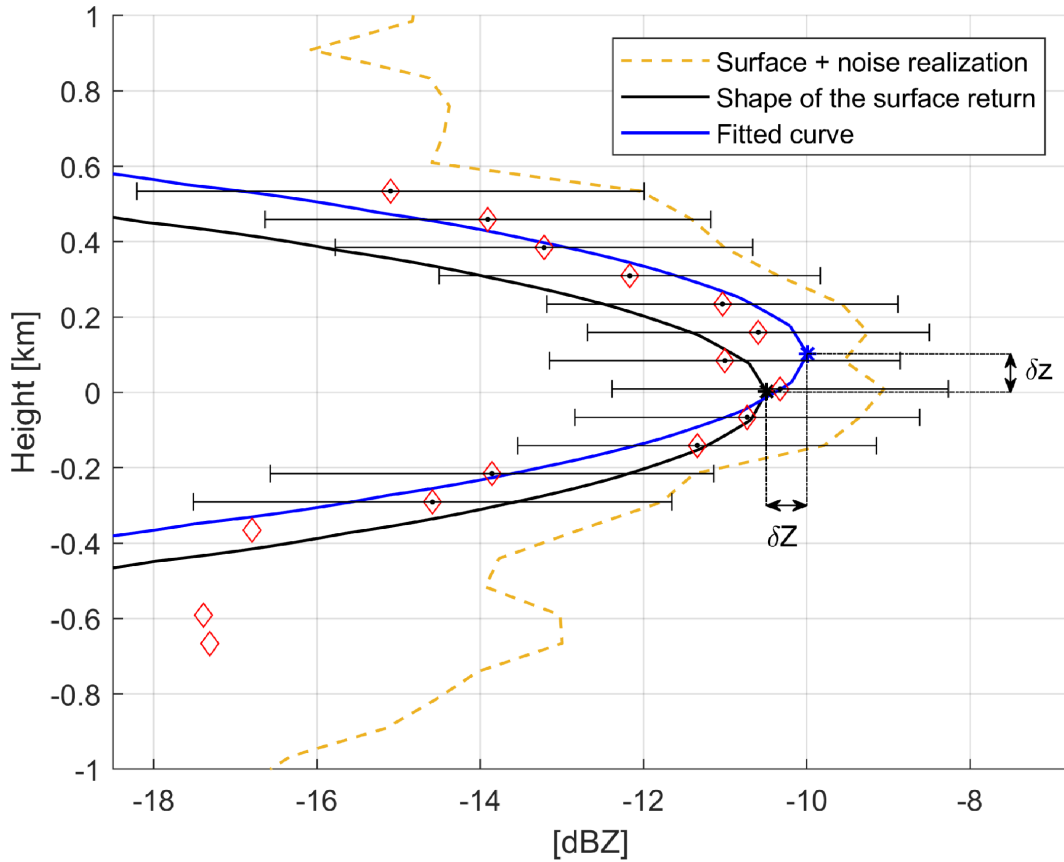
Figure 2. A reflectivity surface profile simulated as observed by the WIVERN radar with the procedure to determine the vertical displacement δz of the peak of the noisy sampled profile with respect to the actual surface peak. The black line represents the ideal shape of the surface return for a 7 dB PNR with its peak highlighted by a black star. The orange dashed line represents a stochastic realization of the same surface return with a -15 dBZ random noise. The red diamonds represent the digitized signal after noise subtraction with the error bars indicating the expected errors in the reflectivity estimates. The black dots insides the red diamonds correspond to the points sampled by the radar that are used for fitting the surface profile. The blue line is the best fitting profile, with the peak highlighted by a blue star. The displacements in height (δz) and in amplitude (δZ) between the black and blue stars are indicative of the uncertainties associated to the clutter characterization.

For instance, more than 36 % and 99 % of the surface peaks exceed -5 dBZ (i.e. PNR=10 dB) for ocean and land surfaces, respectively. Two factors can actually decrease the number of surface returns effectively useful for the calibration:

140   1. the presence of low clouds and precipitation that could perturb the shape of the reflectivity and of the Doppler velocity profile (discussed later in Sect. 3.2);

2. for land surfaces, the failure of the flat surface assumption.
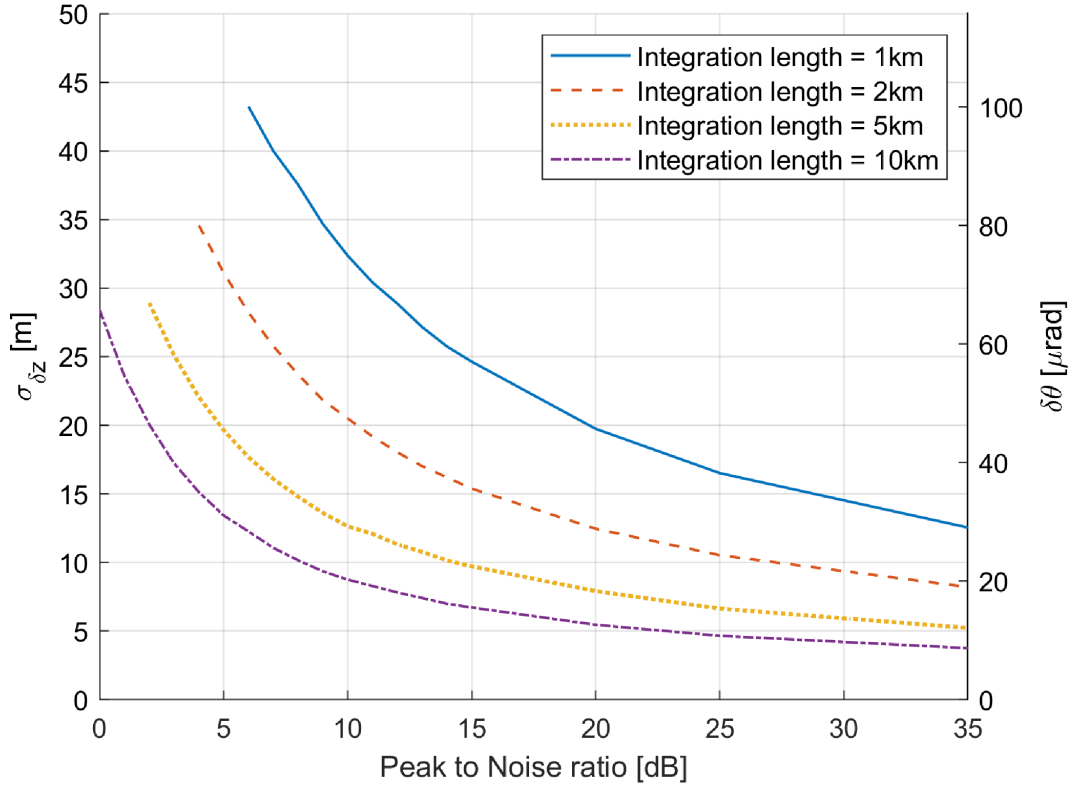
Figure 3. Uncertainty in the elevation mispointing determination by the altimeter mode technique: standard deviations of δz, $\sigma_{\delta z}$ (left axis), and $\delta \theta$ (right axis) as a function of the PNR for different integration lengths, as indicated in the legend. The mean values of δz are negligible for all analysed PNR and integration lengths (not shown). The curves are drawn only for PNRs high enough that more than 80 % of the profiles satisfy the surface detection criterion. See text for details.

In order to assess the first issue, we have recomputed the cdf excluding rays where the hydrometeor signal to clutter ratio (SCR) is higher than -20 dB (dotted lines) and -10 dB (dashed lines) in the 750 m closest to the surface. These conditions ensure that the clutter signal is 100 and 10 times stronger than any perturbing signal produced by the hydrometeors. The presence of low clouds will further reduce the number of useful rays for calibration but such reduction is only of 10 % for SCR lower than -10 dB and of 13 % for SCR lower than -20 dB over ocean. Over land, the reduction is even smaller with 5 % and 10 % for SCR lower than -10 dB and -20 dB, respectively.

For estimating the impact of the second issue see the discussion in Sect. 3.2.1.

3.2 Correction method II: surface Doppler technique

Flat and still surfaces are characterized by a well-determined Doppler velocity profile. But, while the surface reflectivity profiles are independent on the azimuthal scanning angle, the Doppler velocity profiles are azimuthal dependent. Under the assumption
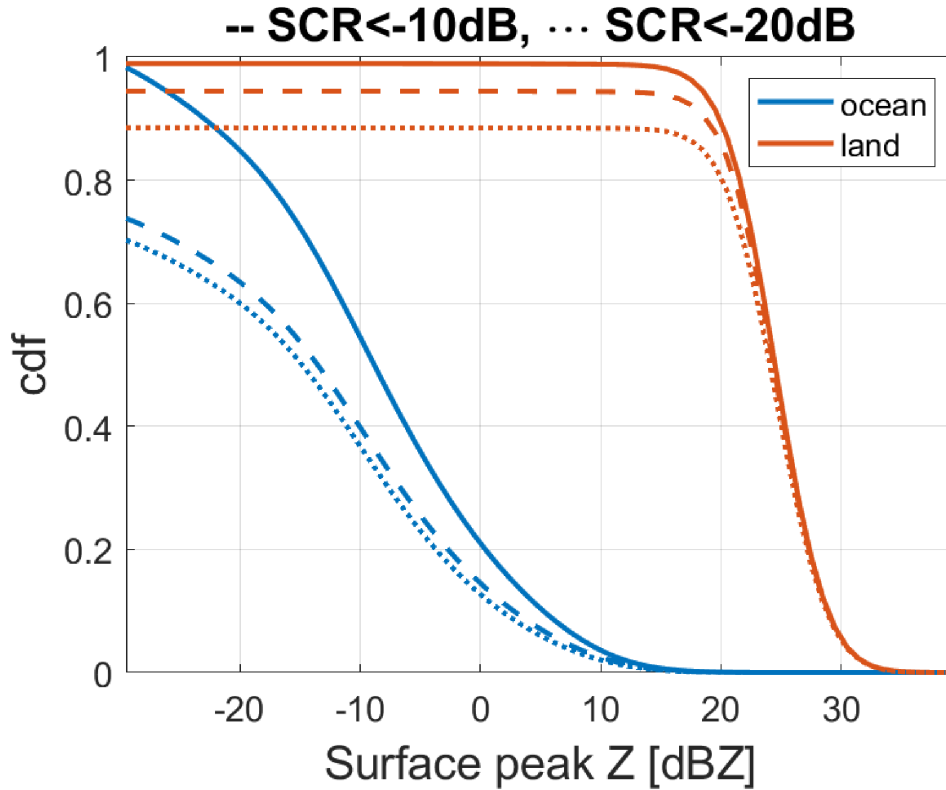
Figure 4. Cumulative distributions of surface reflectivity peaks as expected in WIVERN observations for land (red) and ocean (blue) surfaces. Dashed and dotted lines correspond to rays characterised by decreasing signal to clutter ratios (see the text for more details).

of an homogeneous (i.e. backscattering cross section constant across the footprint) flat and still surface, at side view, the surface Doppler velocity is expected to have 0 m/s at all height bins, whereas, at other azimuthal angles, positive and negative Doppler velocities are expected above and below the surface with 0 m/s only in correspondence to the surface height (black line in Fig. 6). This is the result of the different orientation of the lines of constant Doppler shift induced by v_{SC} (isodops) with respect to the lines with constant range. As demonstrated in Fig. 5, for the two extreme cases of forward (left panel) and side (right panel) views the isodops are parallel and perpendicular, respectively, to the lines of constant range from the radar.

Like done in Sect. 3.1, the Doppler returns as measured by the WIVERN radar are simulated with the noisiness proper to the given PNR and number of independent samples (according to Eq. (16) in Battaglia et al. (2022), diamonds in Fig. 6). Here, a perfect correlation between the V and the H pulse co-polar signals is assumed consistently with low surface LDR values (Wolde et al., 2019). The expected shape (black line) is then fitted through the data that have reflectivites exceeding an SNR of 0 dB via a mean least square technique. The distance of the fitted profile (blue line) from the expected profile at zero height (δv_D) is indicative of the uncertainty in the Doppler velocity error estimation that can be achieved with this methodology.
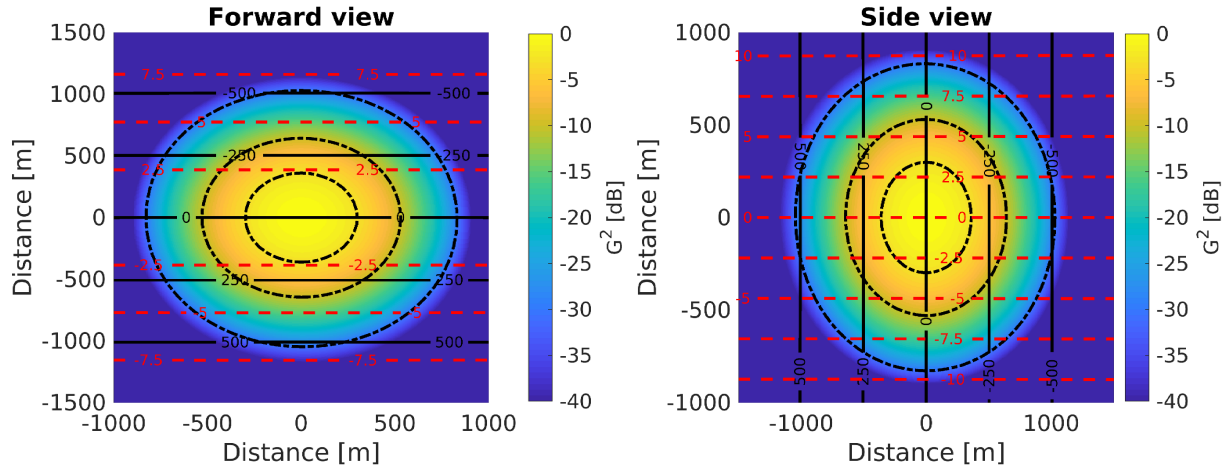
Figure 5. Square of the gain (normalised to 0 dB at boresight) for the WIVERN antenna pattern as derived from a previous study (Lori et al. (2017)) for points within 1500 m from the ground projection of the boresight (used as origin of the coordinate system). Results are reported in correspondence to the forward ($\phi = 0$, left panel) and side ($\phi = 90°$, right panel) view. In both cases the satellite is assumed to move along the y-axis. Contour levels of the satellite velocity along the LOS are plotted as dashed red lines from -10 to 10 m/s with 2.5 m/s separation; contour levels of height above the ground are plotted as black lines from -500 to 500 m with 250 m separation. The dotted black lines correspond to -3, -10 and -30 dB of the normalised square gain.

165   Fig. 7 shows the Doppler velocity uncertainties associated with this method. In this case to reduce the error to values lower than 0.4 m/s is impractical at short integration lengths ($\leq$ 2km) and requires surface with PNR exceeding 10 and 15 dB for integration lengths of 5 and 10 km, respectively. When comparing the curves at different integration lengths, it can be noted that, approximately, the error drops with the square root of the integration length. Therefore this technique seems very promising for correcting mispointing modulated on time scales longer than the antenna rotational period. Surface returns for full rotations in

170   correspondence to clear sky and flat surfaces can be used to fit the mispointing error provided by the expression (1). Because of the numerous number of good calibration points (i.e. "flat" surfaces in clear sky with good PNR) expected to be available in different scans this method will constrain mispointing errors down to less than 0.2 m/s within few turns.

3.2.1   Flat surface approximation

The Advanced Spaceborne Thermal Emission and Reflection Radiometer (ASTER) global digital elevation model (DEM)

175   (https://asterweb.jpl.nasa.gov/GDEM.asp), with a resolution of $1'' \times 1''$ (i.e. 30.9 m $\times$ 30.9 m at the equator), has been used to examine the validity of the flat surface assumption by evaluating the variability of the elevation in areas comparable to that swept by the WIVERN radar footprint with different integration lengths. Boxes with latitudinal extent of $18''$ and longitudinal extents of $18''$, $36''$, $72''$, $90''$, and $180''$ were considered, which corresponds roughly to from no integration to 5 km integration length. The standard deviations of the elevation, σ_{elev}, within each box were then calculated for the entire global data set. Fig. 8
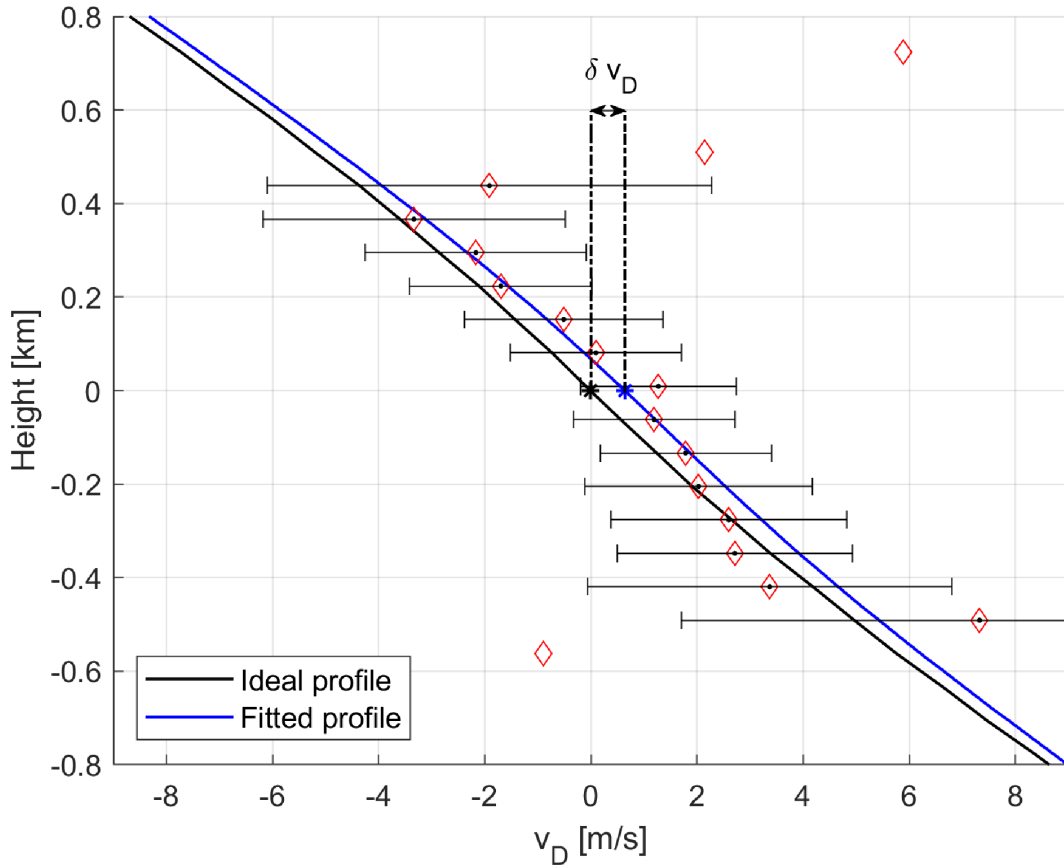
Figure 6. A Doppler velocity profile of the surface simulated for WIVERN observations in the forward direction. The black line represents the ideal Doppler velocity profile without the noise. The red diamonds are the points of the noisy Doppler velocity profile that are oversampled by the radar (one point every 100 m along LOS). The black dots identify the points of the noisy profile with reflectivities above the detection level. Such points are fitted with the shape of the surface return in order to produce the blue line. The Doppler velocities represented by the blue line are the ones retrievable from the radar measurements and they differ from the ideal velocities due to the presence of the noise. δv_D is the velocity shift in correspondence to the surface induced by the noise in the retrieved profile.

180 shows the variation of the cumulative land fraction with σ_{elev}, for the five box sizes adopted. The respective values of σ_{elev} for increasing box size, given in the form (50th percentile, 70th percentile, 90th percentile), are (7.0 m, 12.0 m, 37.3 m), (8.0 m, 14.4 m, 47.1 m), (9.4 m, 17.9 m, 59.5 m), (10.0 m, 19.2 m, 63.5 m), and (12.0 m, 23.6 m, 74.9 m). It is clear that, for a given percentile, the value of σ_{elev} increases as the box size increases. These findings suggest that roughly half of the land surfaces have a variability in elevation less than 10 m within characteristic WIVERN averaging areas. Such surfaces will likely be

185 useful for the calibration methods I-II (Sects. 3.1-3.2), but a dedicated study to properly assess the impact of surface elevation variability is needed.
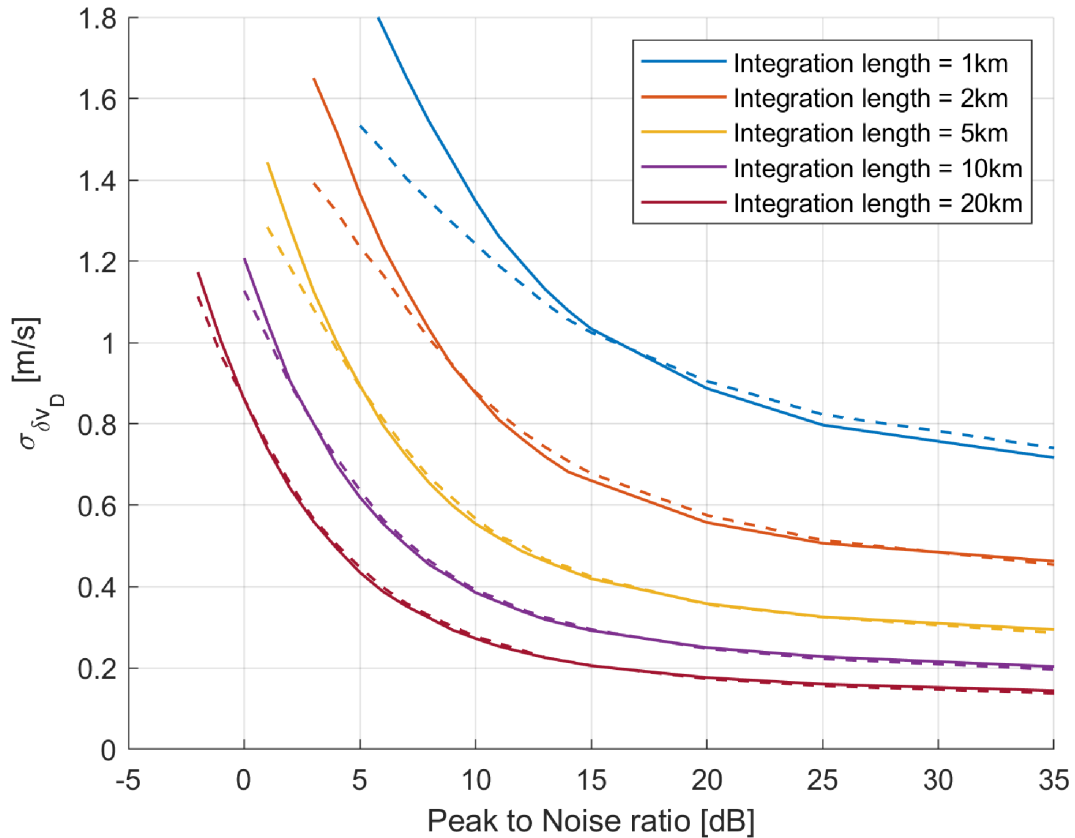
Figure 7. Doppler velocity uncertainty associated with the surface Doppler technique for forward pointing (i.e. azimuthal angle = $0°$, solid lines) and side pointing (i.e. azimuthal angle = $\pm90°$, dashed lines) (but similar results are found for any azimuthal angle). The standard deviations of δv_D is plotted as a function of the PNR for different integration lengths as indicated in the legend. The variability of δv_D decreases as the Peak to Noise Ratio and/or the integration length increase. The mean values of δv_D are negligible for every PNR and every integration length here analysed (not shown). The curves are drawn only for PNRs high enough that more than 80 % of the profiles satisfy the surface detection criterion. See text for details.

A final consideration: generally, ocean surfaces will not appear to have zero Doppler velocities but they will have biases of the order of less than 1 m/s. This is due to the interplay between waves and currents (Chapron et al., 2005; Ardhuin et al., 2019). Here it is assumed that corrections for such effects can be performed based on auxiliary information or that they will average out when considering views from different directions.

3.3 Correction method III: active radar calibrator techniques

The use of active radar calibrators (ARC) is well established for external calibration of SAR instruments. It has been applied for calibrating the TRMM and GPM radars as well (Masaki et al., 2022).
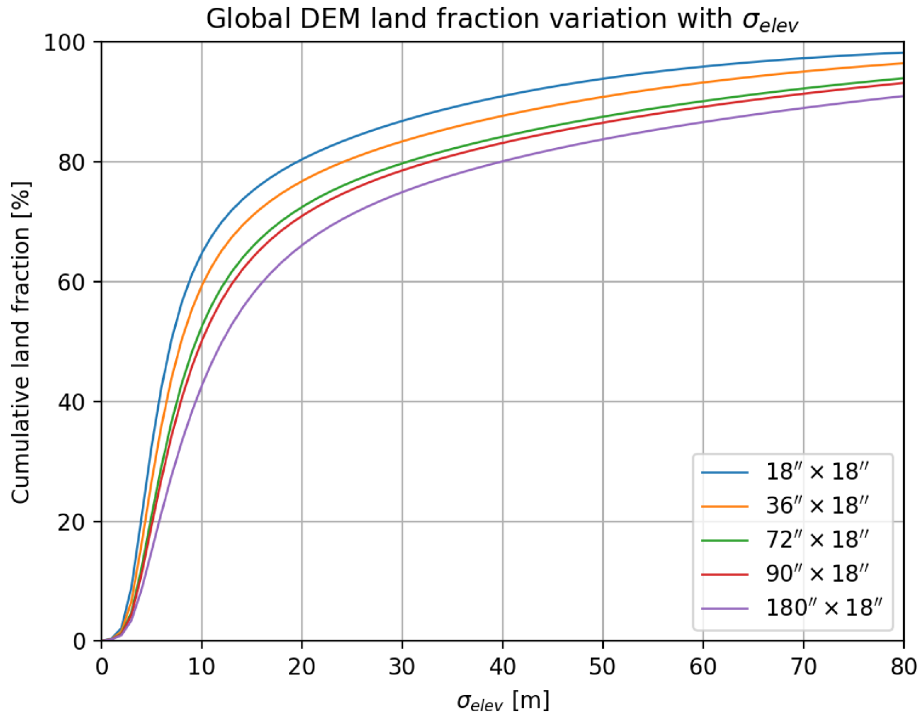
Figure 8. Variation of the cumulative land fraction from the ASTER global digital elevation model (DEM) with σ_{elev} for different latitude/-longitude box sizes. Each coloured line corresponds to a particular longitude × latitude box size (indicated in the legend).

Here we only consider the use of the ARC in receiver mode with extremely high sampling resolution ($\leq 0.1\mu s$). Like in Masaki et al. (2022) we assume the ARC beamwidth of the order of 20°, thus much larger than WIVERN beamwidth. Then, in correspondence of an overpass, if the ARC is pointed toward the satellite, the power received by the ARC at the sampling time t_k, $P_{ARC}(t_k)$, is effectively determined only by the WIVERN Tx antenna pattern. Typically, the signal at the ARC will be detectable for few tenth of milliseconds (see right panels in Fig. 9). Since the velocity of the spacecraft is very low with respect to the scanning velocity of the radar, its effect on the relative motion of the ARC inside the antenna pattern is negligible. Thus, all the possible trajectory of the ARC inside the pattern always look like a slightly bent line extended along the azimuth distance (left panel in Fig. 9).

Note that the radar receiver chain can also be tested by using the radar as an active calibrator (e.g. by sending back to the radar a copy of the signal received by the ARC). With this technique the power received at the WIVERN receiver will depend on the product of the the antenna gain in receiving and transmitting mode and thus will have a higher sensitivity than the method discussed next.
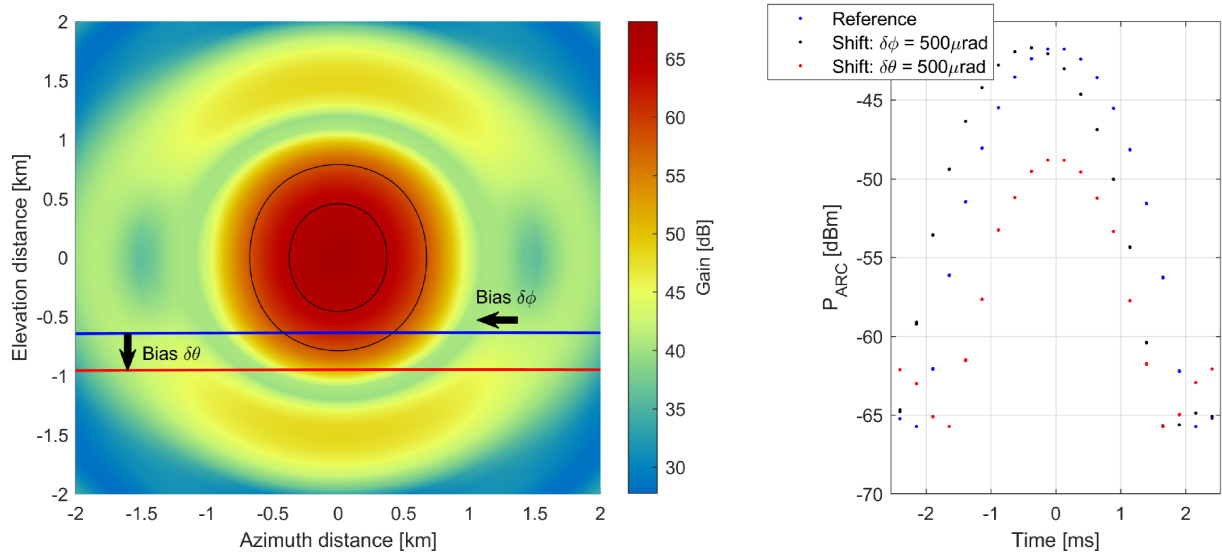
Figure 9. Left panel: example of how the ARC position (expressed in terms of distances at the ground) moves inside the WIVERN antenna pattern when a bias in elevation or in azimuth of 500 μrad is introduced. The satellite is located along the negative y-axis with the antenna pointing forward in the y-direction. The blue line is the position of the ARC for a scanning with a minimum distance between ARC and boresight position of 635 m (reference). The red is the same scan shifted by 500 μrad in elevation bringing the minimum distance between the ARC and the antenna boresight position to 950 m. Black dashed lines correspond to the contour levels of the antenna gain 3 and 10 dB below the maximum gain. Right figure: the ARC received power for the reference (blue) and the scans shifted by 500 μrad in elevation (red) and in azimuth (black). The power received is sampled every 0.1 μs; 3.3μs pulses are transmitted by the radar every 250 μs.

The geolocation of the ARC, the position of the spacecraft, the propagation time of the signal and the time at which the spaceborne radar send the pulses are assumed to be perfectly known. Uncertainty in the knwoledge of those factors affects uncertainty in the mispoiting error detection and in the Doppler velocity correction achieved with the ARC technique.

3.3.1 Elevation mispointing

210   As illustrated in Fig. 9, an elevation mispointing bias moves the apparent motion of the ARC position inside the WIVERN antenna pattern along the elevation direction (y-axis), e.g. from the blue to the red line. Note that uncertainties in the atmospheric refraction between different models (Mangum and Wallace, 2015) are expected to be of the order of 1 arsec (i.e. lower than 5 μrad) and are therefore neglected in this study. Correspondingly, the actual power measured by the ARC, derived by using Friis formula with an ARC gain of 20 dB, changes because of the difference in the antenna pattern. Such change depends on

215   the specific position of the overpass (e.g. on the minimum distance of the boresight position to the ARC) and on the details of the antenna pattern. In order to simulate the capability of the ARC measurement to identify and quantify the mispointing, different possible boresight ground tracks have been simulated (like the blue and the red lines in the left panel of Fig. 9). For

each ARC position at a given elevation distance $\bar{\theta}$, the ARC signal is simulated and compared with the returns sampled at different elevation distances $\bar{\theta} + \Delta\theta$ (with a maximum shift $\Delta\theta$ of $\pm 1000\,\mu rad$ and sampled every $5\,\mu rad$).

The mean square distances of simulated ARC received signals at position $\bar{\theta}$ and $\bar{\theta} + \Delta\theta$ sampled at different time t_k with $k = 1, \ldots, N_t$ is computed as:

$$MSD(\bar{\theta}, \bar{\theta} + \Delta\theta) = \frac{\sqrt{\sum_{k=1}^{N_t} \left(P^{\bar{\theta}}_{ARC}(t_k) - P^{\bar{\theta}+\Delta\theta}_{ARC}(t_k) \right)^2}}{N_t} \qquad -1000\,\mu rad \le \Delta\theta \le 1000\,\mu rad. \qquad (3)$$

All power signals below -80 dBm in the summation have been excluded in order to make sure there will be no effective impact from ARC receiver noise. A (0.5) 1 dB noisiness is introduced in the antenna pattern to account for uncertainties in the antenna pattern. 400 different realizations of the antenna pattern are used to compute the MSD in Eq. (3) so that a distribution of MSD can be derived for each pair $(\bar{\theta}, \bar{\theta} + \Delta\theta)$.

The almost symmetric shape of the antenna pattern causes the similarity between two signals sampled at opposite elevation angles with respect to the boresight (i.e. with $\bar{\theta} = \pm\Delta\theta$). Two examples of the 50th (line) and 5-95th percentiles (shading) of the MSD pdfs are shown in Fig. 10 for $\bar{\theta} = 160\,\mu rad$ (left) and $\bar{\theta} = 480\,\mu rad$ (right). As expected, the minimum is found in correspondence of a shift between the pairs $\Delta\theta$ equal to $0\,\mu rad$ but the interplay between the width of the pdf and the prominence of the local minimum introduces uncertainties in the determination of the mispointing.

When considering an overpass close to the ARC (e.g. $\bar{\theta} = 160\,\mu rad$, left panel), the same MDSs are encountered on a vast interval of $\Delta\theta$, ranging inside the first antenna main lobe in a symmetric way, i.e. with θ between $-\bar{\theta} - \Delta\bar{\theta}$ and $\bar{\theta} + \Delta\bar{\theta}$ with $\Delta\bar{\theta} = 250\mu rad$ for this specific example. When considering ARC positions farther away from the boresight, a second local minimum may form in correspondence of $\Delta\theta = -2 \cdot \bar{\theta}$ (e.g., for $\bar{\theta} = 480\,\mu rad$, the second local minimum is at around $\Delta\theta =$ -960 μrad, right panel).

Left panel of Fig. 11 shows the uncertainty in the elevation mispointing determination as a function of the elevation distance of the ARC from the WIVERN antenna boresight. It is determined by computing for which elevation mispointing the upper 95th percentile, corresponding to the minimum of the MSD (level identified by the red line in Fig. 10), exceeds the lower 5th percentile in the adjacent mispointing angles. The black and the red shading represent the result obtained considering an antenna pattern uncertainty of 0.5 dB and 1.0 dB, respectively. Results show that uncertainty are maximised in correspondence to an overpass of the boresight exactly over the ARC.

Given the fact that there will be multiple overpasses per months (see Fig. 12), it seems realistic to bring this uncertainty down to less than 50 μrad.

3.3.2 Azimuthal mispointing

On the other hand, a mispointing in azimuth does not move the apparent motion of the ARC position inside the WIVERN antenna pattern (Fig. 9), but only translates the received power at the ARC in time. The transmission time and flight time of the radar pulses ($\sim 2.2\,ms$) are well known; excess path lengths in the atmosphere are expected to be less than few meters, thus delays are expected to be of the order of less than $0.01\,\mu s$, negligible in this context (Mangum and Wallace, 2015). The
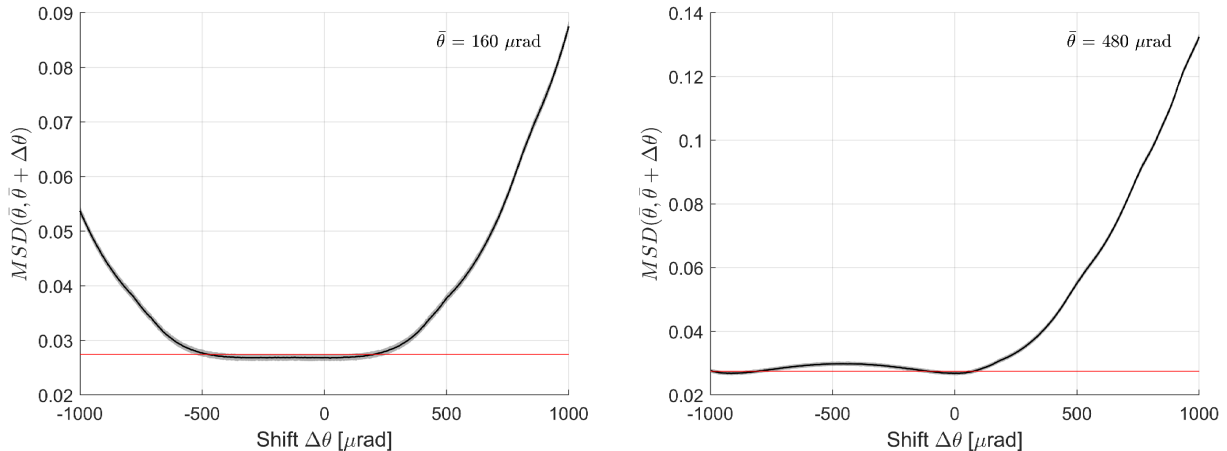
Figure 10. Example of least square distances (the continuous line corresponds to the 50th percentile, while the shading corresponds to the 5th and 95th percentile) for 400 different realizations of the antenna pattern with 1.0 dB of uncertainty as a function of the shift in elevation $\Delta\theta$ for an overpass with antenna boresigth passing at $\bar{\theta} = 160\,\mu$rad (left panel) and at $\bar{\theta} = 480\,\mu$rad from the ARC (right panel).
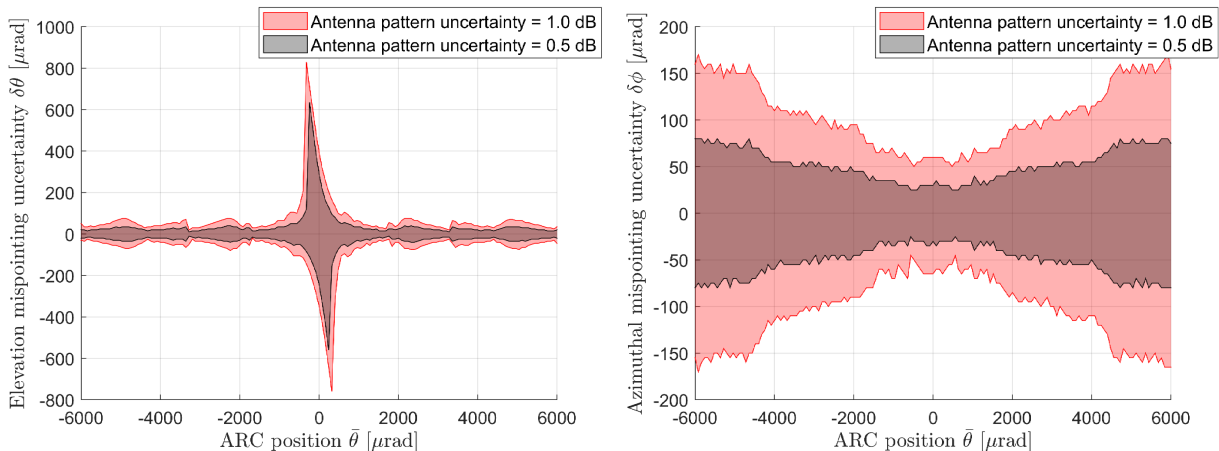
Figure 11. Uncertainty in the elevation (left panel) and azimuthal (right panel) mispointing determination as a function of the minimum ARC elevation distance, $\bar{\theta}$, from the WIVERN antenna boresigth. Cases with 0.5 (black) and 1.0 (red) dB uncertainty in the antenna pattern are shown.

procedure followed for the elevation mispointing is replicated introducing a shift in azimuth, $\Delta\phi$. In this case

$$MSD(\bar{\theta}, \Delta\phi) = \frac{\sqrt{\sum_{k=1}^{N_t} \left(P_{ARC}^{\bar{\theta}}(t_k) - P_{ARC}^{\bar{\theta}}(t_k + \Delta\phi/\Omega_a) \right)^2}}{N_t} \qquad -1000\,\mu rad \leq \Delta\phi \leq 1000\,\mu rad. \qquad (4)$$

As before, pdfs of MSD are computed and an estimate of the uncertainty in the azimuthal mispointing is derived based on percentiles. The right panel of Fig. 11 shows that the closer the overpass is to ARC, the lower is the uncertainty in the azimuthal mispointing determination.

3.3.3 Expected number of useful calibration points as a function of ARC locations

The previous methodology requires the ARC to be positioned in a location within a few km (a few thousand μrad) from the radar boresight location at the ground. To estimate the number of useful calibration points as a function of ARC locations, the WIVERN orbit and boresight positions have been propagated for 50 days. Although the satellite ground track has a repeat cycle of 5 days, the boresight will not trace the same path after this period, thus different regions will be observed within the swath. The simulation rationale consists of selecting a distribution of ARC locations over the region of interest (Fig. 12a) and counting the number of overpasses within a given footprint. A 1 km spacing in latitude and longitude has been selected to generate the ARCs distribution over the region, whereas a time step of 0.5 ms (equal to 250 m along the scan track) has been selected to guarantee a good sampling of the scan track. The simulation has been repeated considering the footprint corresponding to 1, 3, 5 and 10 times the antenna beamwidth.
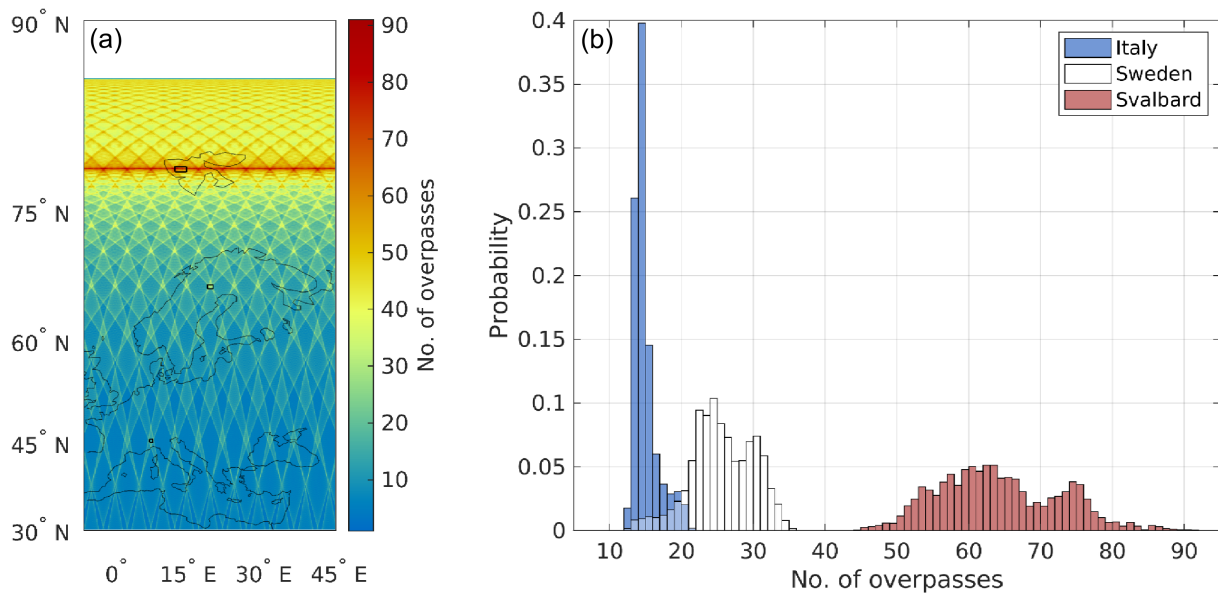
Figure 12. (a) ARCs average number of overpasses within the 10x beamwidth footprint over 10 days. (b) Histogram of the number of overpasses for the selected 50×50 km^2 regions (black rectangles in the left figure).

Fig. 12 shows the average results for a 10 days period obtained from the 50 days simulation. Panel 12a displays the number of overpasses over the selected ARCs for a 10x beamwidth footprint. The image shows several hotspots located at specific latitudes and longitudes, while an optimal longitude-independent cluster of hotspots (red line) exists at around $79°$ of latitude.

Table 2. 10th, 50th and 90th percentiles of the overpasses for the three selected regions over 10 days. The results refer to the overpasses within the footprints corresponding to 1, 3, 5 and 10 times the beamwidth.

	Italy			Sweden			Svalbard		
	10th	50th	90th	10th	50th	90th	10th	50th	90th
1x beamwidth	1	1.4	2	1.4	2.4	3.6	4.6	6.2	8.2
3x beamwidth	3.6	4.4	5.4	5	7.6	10.4	15.2	19	24
5x beamwidth	6.6	7.2	8.6	9	13	16.8	25.9	31.6	39.2
10x beamwidth	13.4	14.4	17.4	20.2	25.2	31.2	53.8	63.2	75.6

Since the enhanced number of overpasses at such locations is generated by the intersections occurring at the lower border of the swath, their positions are around 400 km south of the satellite ground track when it reaches its highest latitude. Three 270 50×50 km^2 regions have been selected around some of the hotspots at latitudes 45°, 66.5° and 78.7°. Panel 12b shows the histogram of the overpasses within these regions, considering the 10x beamwidth footprint. As expected, a greater number of overpasses occurs when moving towards higher latitudes.

Tab. 2 summarizes the results when taking different beamwidths. Clearly, when considering the 10x beamwidth footprint (i.e. within roughly 6000 μrad), a sensible number of overpasses (from at least more than 13 at 45° latitude to more than 53 at 275 78.7° latitude for a 10 days period) is possible over sites whose latitudinal position is properly selected.

3.4 Correction method IV: ascending and descending orbit and ECMWF reference techniques

During a full rotation, the WIVERN instrument will look at the same LOS for azimuthal angles differing by 180°. In such conditions, Eq. (1) predicts that the errors introduced by an azimuthal mispointing will be equal and opposite. But since these are errors on the LOS and the two directions here considered are opposite, it means that the two errors will be identical. Now, for instance, in the part of the orbit closer to the equator, all winds observed at side views (i.e. with $\phi = 90°$, $270°$ where the impact of the azimuthal mispointing is maximum) roughly correspond to the zonal winds. Then, in presence of an azimuthal mispointing that is changing at frequencies much lower than the orbital frequency (f=1.76×10^{-4}s^{-1}), the ascending and descending orbits will see opposite biases for the zonal winds (but this is true also for winds in any other direction, though the effect will reduce to zero when observing the meridional winds because of the $\sin\phi$ modulation). The advantage of side views is also that at such angle the elevation mispointing is irrelevant (because of the $\cos\phi$ modulation). Therefore, in presence of a mispointing $\delta\phi$, the two pdfs of ascending and descending zonal winds collected at side views will be shifted by $\pm v_{SC}\sin\theta\delta\phi$ (i.e. the relative bias between ascending and descending orbits is about 1 m/s for $\delta\phi = 100\,\mu$rad).

Statistically, after several orbits the two pdfs are expected to converge to the same pdf under the assumption that the zonal winds at local times differing by 12 h are the same. Is this assumption correct? In this case, any discrepancy between the two pdfs will be a signature of an azimuthal mispointing. But what is the sensitivity of this methodology? i.e. how long is it necessary to average in order to overcome the natural variability and what is the detectable bias for a given time scale?

Alternatively, all H-LOS winds can be compared with ECMWF background forecast winds, that have been proved to be unbiased (biases are ≤ 0.3 m/s in zonal wind and ≤ 0.15 m/s in meridional winds), have good precision (standard deviations of the order of 2.5 m/s mostly because of unresolved small scale variability, Rennie (2022)) and have been exploited to correct Aelous wind biases (Weiler et al., 2021). Each WIVERN H-LOS wind can be subtracted from the ECMWF reference. If WIVERN quality controlled winds are unbiased, then the distribution of the difference should have zero mean; otherwise, the bias could be estimated with an error which will be equal to $\sigma_{WIVERN-ECMWF}/\sqrt{N_{winds}}$ where $\sigma_{WIVERN-ECMWF}$ is the standard deviation of the distribution of the differences and N_{winds} is the number of independent winds.

3.4.1 CloudSat-based analysis

To address these questions the dataset produced in Tridon et al. (2023) that combines the CloudSat reflectivity observations and the ECMWF winds has been exploited. Since CloudSat is orbiting in a sun-synchronous polar orbit like the one foreseen for WIVERN, the winds sampled in the ascending and descending orbits have the same statistical variability expected for WIVERN.

Figure 13 shows an example of simulation of WIVERN measurements from a portion of CloudSat orbit through a North-Eastern Atlantic widespread low which brought a significant amount of precipitation and high winds over Ireland on the 19th February 2007. The CloudSat reflectivity curtain (panel 13a) is combined with the corresponding ECMWF wind reanalysis (panel 13b) to simulate the slant reflectivity (panel 13c) and Doppler velocity (panel 13d) curtains that would be observed by WIVERN at side-view ($\phi = 90°$). Because of the slant incidence angle, the WIVERN surface reflectivity is much lower than
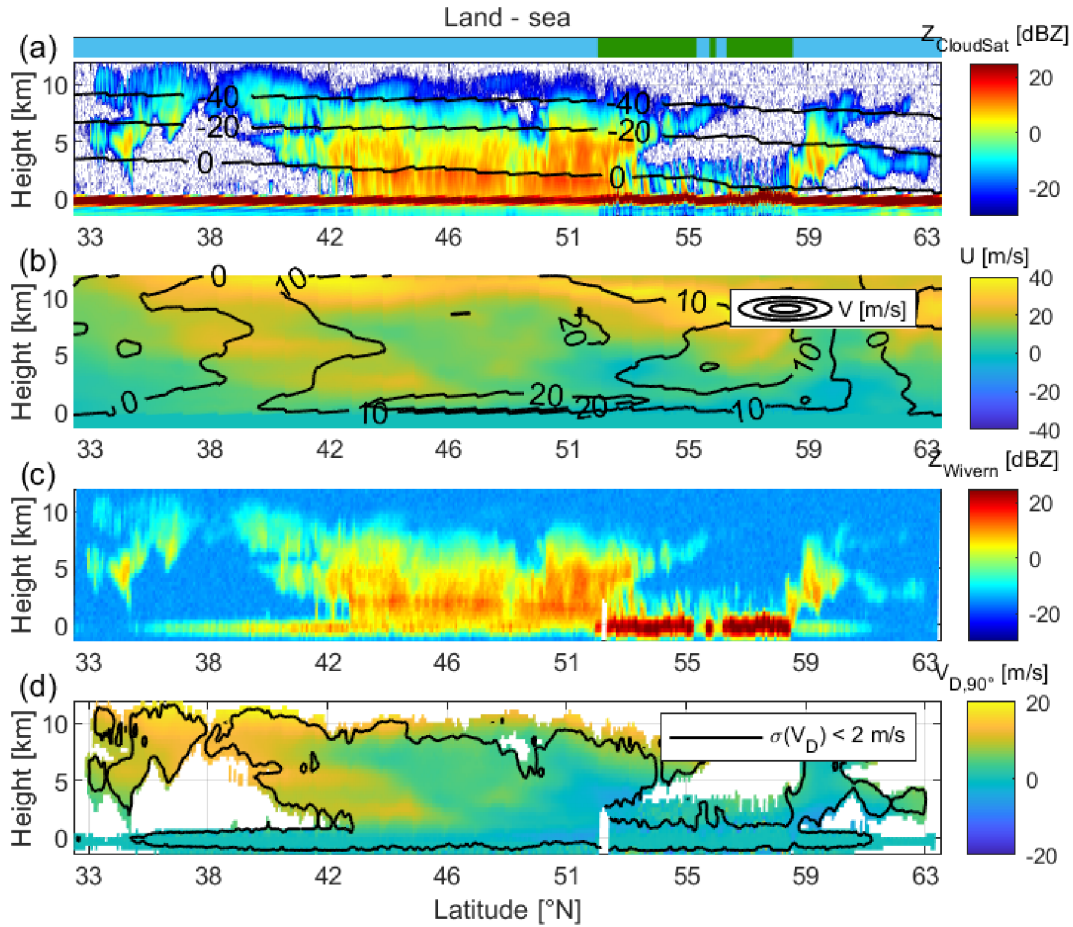
Figure 13. (a) CloudSat reflectivity of a frontal system over East Atlantic and British Isles, and ECMWF temperature contours. (b) Corresponding zonal (colors) and meridional (contours) ECMWF winds. (c) Simulated Wivern reflectivity at 10 km resolution. (d) Simulated side-view Wivern Doppler velocity at 10 km resolution with a contour showing areas with an accuracy associated to the radar estimator better than 2 m s^{-1}.

that of CloudSat apart from over land (see land/sea flag at the top of panel a). In panel 13d, the black contour highlights the areas where the WIVERN Doppler velocity accuracy would be better than 2 m s^{-1}.

Our method follows the following steps:

1. the dataset has been divided in ascending (A) and descending (D) orbits for latitudes between -65° and 65°;

2. histograms of WIVERN LOS winds when looking sideways to the right/left of satellite in A/D orbits (roughly corresponding to zonal winds) have been accumulated at different heights; only winds where clouds are present and produce

315   an SNR larger than -4 dB have been considered; random noise is added to each observation according to the expected
       error computed from the radar simulator (formula 16 in Battaglia et al. (2022)) for integration lengths of 10 km.

   3. ensemble of pdfs of WIVERN "zonal winds" are produced for different integration periods.

   4. Jensen-Shannon distances (like in Battaglia et al. (2023)) between ascending and descending pdfs computed in 3 and for
      A/D pdfs shifted by different wind biases (e.g. ± 2 m/s corresponding to azimuth biases of 400 μrad).

320   5. threshold values expressed in terms of integration time or number of measured winds where different bias levels become
       detectable for 4. are computed (like in Battaglia et al. (2023)).
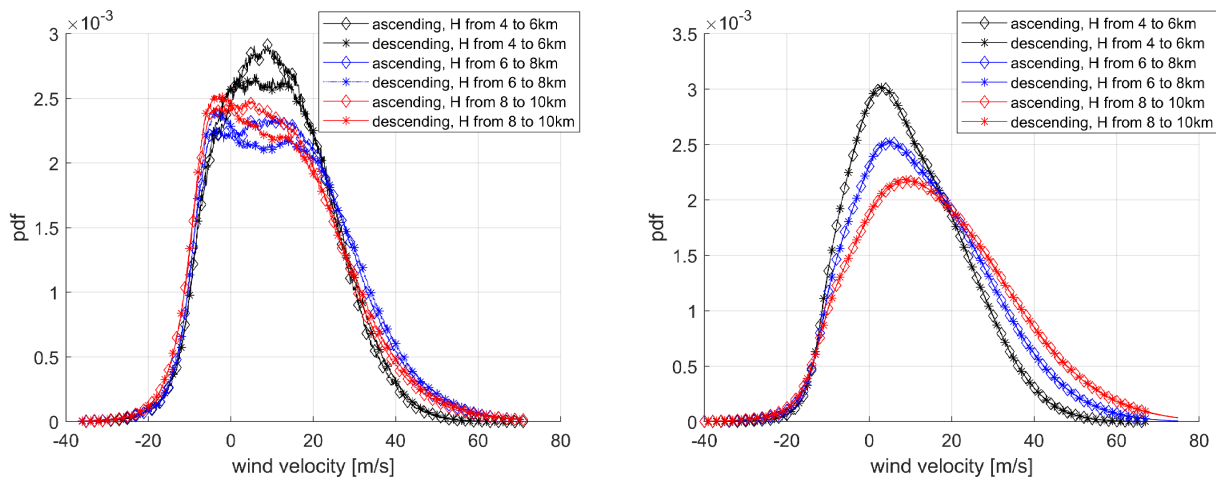
Figure 14. Pdfs of A (diamond marker) and D (star "*" marker) in-cloud horizontal winds retrieved by Wivern when looking sideways (left panel) and all-sky conditions horizontal winds at Wivern side view (right panel). In the left panel, only points characterized by a Doppler velocity accuracy better than 4 m/s are considered. The histograms have been generated with points sampled at latitudes within $\pm 65°$ and at different altitude intervals, as indicated in the legend. The pdfs have been generated with 270 (in-cloud winds) and 365 (all-sky winds) days of data.

   Pdfs of in-cloud horizontal winds retrieved by WIVERN when looking sideways are shown in the left panel of Fig. 14 for A/D orbits (diamond/star markers) and for different height ranges as indicated in the legend. The same plot is repeated on the right hand side considering all-sky condition winds. In the latter condition, A and D wind distributions looks pretty much
325 identical. However, when considering only in-cloud winds, the two distributions take different shapes, suggesting the existence of a diurnal cycle (A and D winds are sampled twelve hours apart) affecting in-cloud winds. This result makes the option of identifying azimuthal mispointing only by using WIVERN ascending and descending measurements challenging because the pdfs of A/D in-cloud winds are intrinsically different and therefore large biases in the winds (typically of the order of 1 m/s, i.e. $\phi \approx 200\mu$rad) are needed to see a neat separation between the two pdfs for accumulation times of at least 10-15 days (not
330 shown).

On the other hand, when considering the ECMWF as a reference, Fig. 15 demonstrates that the histogram of the differences for the side winds has a standard deviation of the order of 3.66 m/s with an average of about 80,000 winds per day. In this case, only WIVERN's wind measurements characterized by a SNR higher than 0 dB have been taken into account. Because of this large amount of winds, this demonstrates that the error on the estimate of the azimuthal bias will become negligible (≤ 0.2m/s) already after few minutes. The real limit becomes in this case the assumption that the reference ECMWF winds are unbiased. The validity of such assumption applies on global averages over few days with an upper limit for the bias of circa 0.3 m/s. Note that the same reasoning can be applied to the forward/backward line of sight winds and therefore to the elevation biases.
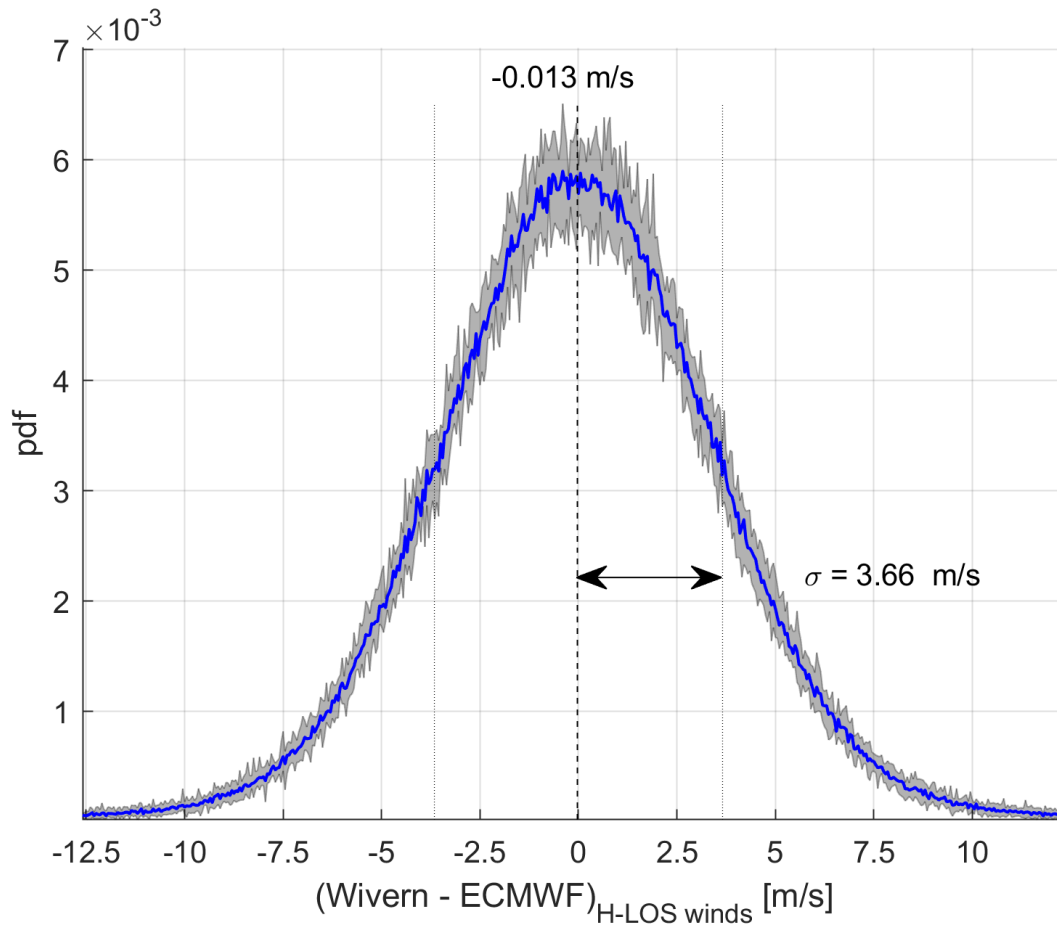
Figure 15. Pdf of the difference between the winds retrieved by Wivern (LOS) at side view and the ECMWF winds. The pdf have been generated with 801,474 points, all with an SNR larger than 0 dB, collected during a period of 10 days (blue line). The envelope of the one day pdfs collected in each of those 10 days is also shown (gray shading).

4 Summary and conclusions

Different methodologies for correcting mispointing errors in conically scanning Doppler velocity measurements (with focus at the WIVERN configuration, currently under study as one of the Earth Explorer 11 candidate missions) have been discussed. Results show that:

– The use of radar in "altimeter" mode is very robust for identifying elevation mispointing on very short time scales (few ms). Depending on the surface peak strength and the integration length, different levels of correction can be achieved; e.g. with a 10 dB peak to noise ratio less than 20 μrad (50 μrad) can be achieved at 10 km (2 km) integration length. This value corresponds to velocity errors smaller than 0.12 m/s (0.28 m/s). The methodology is limited by the flat surface assumption and by the absence of low atmospheric targets that may contaminate the surface signal. Proper screening to identify these situations must be performed before hand.

– The surface Doppler velocity profile can be used for correcting both elevation and azimuthal mispointing but with generally worse performances than the previous method. With a 10 dB surface peak to noise ratio errors of 0.4 m/s (0.9 m/s) can be achieved at 10 km (2 km) integration length. The method is likely to produce accurate pointing corrections when making use of the clear sky, high peak to noise ratio flat surfaces encountered across several antenna rotations. Limitations similar to the previous method apply in this instance; additionally, for ocean surfaces, the potential bias introduced to the Doppler velocity by waves and currents must be accounted for.

– The use of an active radar calibrator is effective in identifying slowly changing mispointing errors (biases) larger than about 50 μrad when considering multiple overpasses over week-long periods with the error mainly driven by the knowledge of the details of the antenna pattern. The location of the ARC can be optimally chosen based on the orbit details, with the goal of maximising the number of overpasses.

– Winds measured by WIVERN in ascending and descending orbits can be used to detect azimuthal biases but only for large biases (of the order of 200 μrad) on time scale longer than 10 days. On the other hand, because of the huge number of WIVERN winds measurements collected every day, the comparison of the Level 2 WIVERN HLOS wind to a state-of-the-art data assimilation system and forecast model like provided by ECMWF via the so-called O-B (observation - background) technique is extremely effective in determining biases. The method is practically only limited by time and spatial scales at which the reference model can be considered unbiased.

Future work should address the impact of the instrument footprint variability of the surface σ_0 (e.g. due to differential attenuation or by surface height variability) for methodology 1 and 2. The impact of waves and currents on the Doppler velocity measurements should also be established at this high frequency and at slant incidence angles.

Appendix A: Effect of a scan-axis mounting offset

In general, the effect of a scan-axis mounting offset can be considered as well. Let A_{roll}, A_{pitch}, A_{yaw} be the roll, pitch and yaw angles, respectively, which characterize the scan-axis mounting offset. We can assume that these angles are constant in time. The offset will generate a bias in the elevation and azimuthal angles with respect to the case where no offset is present; the mispointing in elevation and azimuthal will be time-dependent with harmonics of the antenna angular velocity, Ω_a, according to:

$$\Delta\theta(t) \quad = \quad -A_{roll}\sin(\Omega_a\,t) + A_{pitch}\cos(\Omega_a\,t) \tag{A1}$$
$$\Delta\phi(t) \quad = \quad -\frac{\cos(\Omega_a\,t)}{\tan(\theta)}A_{roll} - \frac{\sin(\Omega_a\,t)}{\tan(\theta)}A_{pitch} + A_{yaw} \tag{A2}$$

The offset angles can be derived as following.

- Since offset in roll and pitch induce Ω_a-harmonic mispointing in elevation, A_{roll} and A_{pitch} can be identified with method #1. The bias in altitude of the surface position, δz, can be averaged over a period long enough in order to cancel out the mispointing in elevation induced by the antenna (effective at higher frequencies). Then, A_{roll} and A_{pitch} can be retrieved from Eq. (2) by looking at the δz at forward/backward and side views for A_{roll} and A_{pitch}, respectively.

- A_{yaw} can be handled as a constant azimuthal mispointing, and thus its effect on the Doppler velocity can be corrected adopting method #2.

The assumption that the scan-axis mounting offset is constant is usually valid for errors in the original mounting or by misalignments generated by post-launch conditions. Finally, note that Eqs. (A1-A2) allows to convert a generic perturbation in roll, pitch and yaw of the platform (e.g. inherent to the spacecraft attitude control) into a mispointing in the antenna azimuth and elevation.

Author contributions. FES performed most of the simulations and the analyses. AB wrote most of the text and has defined the project. FT performed the analysis on the statistics of useful surface return and provided the simulations for the CloudSat based analysis. PM performed the analysis on the expected number of overpasses on different ARC locations. RD performed the analysis on the flat surface approximation. AI contributed to the discussion and the review of the paper.

Competing interests. The authors declare that they have no conflict of interest.

Acknowledgements. This work was supported in part by the European Space Agency under the activity WInd VElocity Radar Nephoscope (WIVERN) Phase 0 Science and Requirements Consolidation Study, ESA Contract Number 4000136466/21/NL/LF. AB's work was funded

by Compagnia di San Paolo. FES's work was conducted during and with the support of the Italian national inter-university PhD course in Sustainable Development and Climate change (link: www.phd-sdc.it). This research used the Mafalda cluster at Politecnico di Torino.

References

Ardhuin, F., Brandt, P., Gaultier, L., Donlon, C., Battaglia, A., Boy, F., Casal, T., Chapron, B., Collard, F., Cravatte, S., Delouis, J.-M., DeWitte, E., Dibarboure, G., Engen, G., Johnsen, H., Lique, C., PacoLopez-Dekker, Maes, C., Martin, A., Mari, L., Menemenlis, D., Nouguier, F., Peureux, C., Rampal, P., Ressler, G., Rio, M.-H., Rommen, B., Shutler, J. D., Suess, M., Tsamados, M., Ubelmann, C., van Sebille, E., van der Vorst, M., and Stammer, D.: SKIM, a candidate satellite mission exploring global ocean currents and waves, Frontiers, 2019.

Battaglia, A. and Kollias, P.: Using ice clouds for mitigating the EarthCARE Doppler radar mispointing, IEEE Trans. Geosci. Remote Sens., 53, 2079–2085, doi: 10.1109/TGRS.2014.2353219, 2014.

Battaglia, A., Tanelli, S., and Kollias, P.: Polarization Diversity for Millimeter Spaceborne Doppler Radars: An Answer for Observing Deep Convection?, J. Atmos. Ocean. Tech., 30, 2768–2787, https://doi.org/10.1175/JTECH-D-13-00085.1, 2013.

Battaglia, A., Wolde, M., D'Adderio, L. P., Nguyen, C., Fois, F., Illingworth, A., and Midthassel, R.: Characterization of Surface Radar Cross Sections at W-Band at Moderate Incidence Angles, IEEE Trans. Geosci. Remote Sens., 55, 3846–3859, 10.1109/TGRS.2017.2682423, 2017.

Battaglia, A., Dhillon, R., and Illingworth, A.: Doppler W-band polarization diversity space-borne radar simulator for wind studies, Atm. Meas. Tech., 11, 5965–5979, https://doi.org/10.5194/amt-11-5965-2018, 2018.

Battaglia, A., Kollias, P., Dhillon, R., Roy, R., Tanelli, S., Lamer, K., Grecu, M., Lebsock, M., Watters, D., Mroz, K., Heymsfield, G., Li, L., and Furukawa, K.: Spaceborne Cloud and Precipitation Radars: Status, Challenges, and Ways Forward, Reviews of Geophysics, 58, e2019RG000 686, https://doi.org/10.1029/2019RG000686, e2019RG000686 10.1029/2019RG000686, 2020.

Battaglia, A., Martire, P., Caubet, E., Phalippou, L., Stesina, F., Kollias, P., and Illingworth, A.: Observation error analysis for the WInd VElocity Radar Nephoscope W-band Doppler conically scanning spaceborne radar via end-to-end simulations, Atmospheric Measurement Techniques, 15, 3011–3030, https://doi.org/10.5194/amt-15-3011-2022, 2022.

Battaglia, A., Scarsi, F. E., Mroz, K., and Illingworth, A.: In orbit cross-calibration of millimeter conically scanning spaceborne radars, Atmospheric Measurement Techniques, 16, 3283–3297, https://doi.org/10.5194/amt-16-3283-2023, 2023.

Chapron, B., Collard, F., and Ardhuin, F.: Direct measurements of ocean surface velocity from space: Interpretation and validation, Journal of Geophysical Research: Oceans, 110, https://doi.org/https://doi.org/10.1029/2004JC002809, 2005.

Doviak, R. J. and Zrnić, D. S.: Doppler Radar and Weather Observations, Academic Press, 1993.

Durden, S. L., Siqueira, P. R., and Tanelli, S.: On the Use of Multiantenna Radars for Spaceborne Doppler Precipitation Measurements, IEEE Geosci. Remote Sens. Lett., 4, 181–183, https://doi.org/10.1109/LGRS.2006.887136, 2007.

ESA: ADM-Aeolus Science Report, Tech. rep., ESA SP-1311, available at https://esamultimedia.esa.int/multimedia/publications/SP-1311/SP-1311.pdf, 2008.

ESA: WIVERN Report for Assessment, Tech. rep., ESA-EOPSM-WIVE-RP-4375, available at https://eo4society.esa.int/event/earth-explorer-11-user-consultation-meeting/, 2023.

Geer, A. J., Baordo, F., Bormann, N., Chambon, P., English, S. J., Kazumori, M., Lawrence, H., Lean, P., Lonitz, K., and Lupu, C.: The growing impact of satellite observations sensitive to humidity, cloud and precipitation, Quart. J. Roy. Meteor. Soc., 143, 3189–3206, https://doi.org/10.1002/qj.3172, 2017.

Illingworth, A., Battaglia, A., and Delanoe, J.: WIVERN: An ESA Earth Explorer Concept to Map Global in-Cloud Winds, Precipitation and Cloud Properties, in: 2020 IEEE Radar Conference (RadarConf20), pp. 1–6, https://doi.org/10.1109/RadarConf2043947.2020.9266286, 2020.

Illingworth, A. J., Battaglia, A., Bradford, J., Forsythe, M., Joe, P., Kollias, P., Lean, K., Lori, M., Mahfouf, J.-F., Melo, S., Midthassel, R., Munro, Y., Nicol, J., Potthast, R., Rennie, M., Stein, T. H. M., Tanelli, S., Tridon, F., Walden, C. J., and Wolde, M.: WIVERN: A New Satellite Concept to Provide Global In-Cloud Winds, Precipitation, and Cloud Properties, Bull. Amer. Met. Soc., 99, 1669–1687, https://doi.org/10.1175/BAMS-D-16-0047.1, 2018.

Kobayashi, S., Kumagai, H., and Kuroiwa, H.: A Proposal of Pulse-Pair Doppler Operation on a Spaceborne Cloud-Profiling Radar in the W Band, J. Atmos. Ocean. Tech., 19, 1294 – 1306, https://doi.org/10.1175/1520-0426(2002)019<1294:APOPPD>2.0.CO;2, 2002.

Kollias, P., Tanelli, S., Battaglia, A., and Tatarevic, A.: Evaluation of EarthCARE Cloud Profiling Radar Doppler Velocity Measurements in Particle Sedimentation Regimes, J. Atmos. Ocean. Tech., 31, 366–386, https://doi.org/10.1175/JTECH-D-11-00202.1, 2014.

Kollias, P., Battaglia, A., Lamer, K., Treserras, B. P., and Braun, S. A.: Mind the Gap - Part 3: Doppler Velocity Measurements From Space, Frontiers in Remote Sensing, 3, https://doi.org/10.3389/frsen.2022.860284, 2022.

Kollias, P., Puidgomènech Treserras, B., Battaglia, A., Borque, P. C., and Tatarevic, A.: Processing reflectivity and Doppler velocity from EarthCARE's cloud-profiling radar: the C-FMR, C-CD and C-APC products, Atm. Meas. Tech., 16, 1901–1914, https://doi.org/10.5194/amt-16-1901-2023, 2023.

Lori, M., Pfeiffer, E. K., Cardoso, C., de Rijk, E., Caubet, E., Battaglia, A., Trenta, D., and van der Vorst, M.: The DORA conical scan antenna, in: 38th ESA Antenna Workshop on Innovative Antenna Systems and Technologies for Future Space Missions 3-6 October 2017, Noordwijk, The Netherlands, 2017.

Lux, O., Lemmerz, C., Weiler, F., Kanitz, T., Wernham, D., Rodrigues, G., Hyslop, A., Lecrenier, O., McGoldrick, P., Fabre, F., Bravetti, P., Parrinello, T., and Reitebuch, O.: ALADIN laser frequency stability and its impact on the Aeolus wind error, Atm. Meas. Tech., 14, 6305–6333, https://doi.org/10.5194/amt-14-6305-2021, 2021.

Mangum, J. G. and Wallace, P.: Atmospheric Refractive Electromagnetic Wave Bending and Propagation Delay, Publications of the Astronomical Society of the Pacific, 127, 74–91, http://www.jstor.org/stable/10.1086/679582, 2015.

Masaki, T., Iguchi, T., Kanemaru, K., Furukawa, K., Yoshida, N., Kubota, T., and Oki, R.: Calibration of the Dual-Frequency Precipitation Radar Onboard the Global Precipitation Measurement Core Observatory, IEEE Trans. Geosci. Remote Sens., 60, 1–16, https://doi.org/10.1109/TGRS.2020.3039978, 2022.

Meneghini, R. and Kozu, T.: Spaceborne weather radar, Artech House, 1990.

Polverari, F., Portabella, M., Lin, W., Sapp, J. W., Stoffelen, A., Jelenak, Z., and Chang, P. S.: On High and Extreme Wind Calibration Using ASCAT, IEEE Trans. Geosci. Remote Sens., 60, 1–10, https://doi.org/10.1109/TGRS.2021.3079898, 2022.

Rennie, M.: The NWP impact of Aeolus Level-2B winds at ECMWF (v5.0, 10 August 2022), Disc contract technical note, https://confluence.ecmwf.int/display/AEOL/L2B+team+technical+reports+and+relevant+papers, 2022.

Rennie, M. P., Isaksen, L., Weiler, F., de Kloe, J., Kanitz, T., and Reitebuch, O.: The impact of Aeolus wind retrievals on ECMWF global weather forecasts, Quart. J. Roy. Meteor. Soc., 147, 3555–3586, https://doi.org/10.1002/qj.4142, 2021.

Rizik, A., Battaglia, A., Tridon, F., Scarsi, F. E., Kötsche, A., Kalesse-Los, H., Maahn, M., and Illingworth, A.: Impact of Crosstalk on Reflectivity and Doppler Measurements for the WIVERN Polarization Diversity Doppler Radar, IEEE Transactions on Geoscience and Remote Sensing, 61, 1–14, https://doi.org/10.1109/TGRS.2023.3320287, 2023.

Stoffelen, A., Pailleux, J., Kallen, E., Vaughan, J. M., Isaksen, L., Flamant, P., Wergen, W., Andersson, E., Schyberg, H., Culoma, A., Meynart, R., Endemann, M., and Ingmann, P.: The Atmospheric Dynamics Mission for Global Wind Field Measurement, Bull. Amer. Met. Soc., 86, 73–87, 2005.

470 Stoffelen, A., Benedetti, A., Borde, R., Dabas, A., Flamant, P., Forsythe, M., Hardesty, M., Isaksen, L., Källén, E., Körnich, H., Lee, T., Reitebuch, O., Rennie, M., Riishøjgaard, L.-P., Schyberg, H., Straume, A. G., and Vaughan, M.: Wind Profile Satellite Observation Requirements and Capabilities, Bull. Amer. Met. Soc., 101, E2005 – E2021, https://doi.org/10.1175/BAMS-D-18-0202.1, 2020.

Sy, O. O., Tanelli, S., Takahashi, N., Ohno, Y., Horie, H., and Kollias, P.: Simulation of EarthCARE Spaceborne Doppler Radar Products Using Ground-Based and Airborne Data: Effects of Aliasing and Nonuniform Beam-Filling, IEEE Trans. Geosci. Remote Sens., 52,

475 1463–1479, https://doi.org/10.1109/TGRS.2013.2251639, 2014.

Tanelli, S., Im, E., Durden, S. L., Facheris, L., and Giuli, D.: The Effects of Nonuniform Beam Filling on Vertical Rainfall Velocity Measurements with a Spaceborne Doppler Radar, J. Atmos. Ocean. Tech., 19, 1019–1034, https://doi.org/10.1175/1520-0426(2002)019<1019:TEONBF>2.0.CO;2, 2002.

Tanelli, S., Im, E., Durden, S. L., Facheris, L., Giuli, D., and Smith, E.: Rainfall Doppler velocity measurements from spaceborne radar:

480 overcoming nonuniform beam filling effects, J. Atmos. Ocean. Tech., 21, 27–44, doi: 10.1175/1520-0426, 2004.

Tanelli, S., Durden, S. L., and Johnson, M. P.: Airborne Demonstration of DPCA for Velocity Measurements of Distributed Targets, IEEE Geosci. Remote Sens. Lett., 13, 1415–1419, https://doi.org/10.1109/LGRS.2016.2581174, 2016.

Tridon, F., Battaglia, A., Rizik, A., Scarsi, F. E., and Illingworth, A.: Filling the Gap of Wind Observations Inside Tropical Cyclones, Earth and Space Science, 10, e2023EA003 099, https://doi.org/10.1029/2023EA003099, e2023EA003099 2023EA003099, 2023.

485 Weiler, F., Rennie, M., Kanitz, T., Isaksen, L., Checa, E., de Kloe, J., Okunde, N., and Reitebuch, O.: Correction of wind bias for the lidar on board Aeolus using telescope temperatures, Atmospheric Measurement Techniques, 14, 7167–7185, https://doi.org/10.5194/amt-14-7167-2021, 2021.

Wolde, M., Battaglia, A., Nguyen, C., Pazmany, A. L., and Illingworth, A.: Implementation of polarization diversity pulse-pair technique using airborne W-band radar, Atm. Meas. Tech., 12, 253–269, https://doi.org/10.5194/amt-12-253-2019, 2019.

490 Zrnic, D. S.: Simulation of weatherlike Doppler spectra and signal, J. Appl. Meteorol., 14, 619–620, 1975.